Editors' Suggestion

Transient three-dimensional structural dynamics in 1*T*-$TaSe_2$

Shaozheng Ji,[1] Oscar Grånäs,[2] Kai Rossnagel,[3,4] and Jonas Weissenrieder[1,*]

[1]*Materials and Nano Physics, School of Engineering Sciences, KTH Royal Institute of Technology, SE-100 44 Stockholm, Sweden*
[2]*Materials Theory, Department of Physics and Astronomy, Uppsala University, 751 20 Uppsala, Sweden*
[3]*Institut für Experimentelle und Angewandte Physik, Christian-Albrechts-Universität zu Kiel, D-24098 Kiel, Germany*
[4]*Ruprecht-Haensel-Labor, Deutsches Elektronen-Synchrotron DESY, D-22607 Hamburg, Germany*

(Received 22 October 2019; revised manuscript received 30 December 2019; accepted 19 February 2020; published 5 March 2020)

We report on thermal and optically driven transitions between the commensurate (C) and incommensurate (IC) charge-density wave (CDW) phases of 1*T*-$TaSe_2$. Optical excitation results in suppression of the C-CDW on a subpicosecond timescale. The optically driven C to IC transition involves a short-lived (∼1 ps) unreconstructed phase. Nucleation of an IC phase stacking order is observed already at ∼4 ps following photoexcitation. The short timescales involved in establishing the stacking order implies that the nucleation of the IC phase is influenced by the local geometry of the adjacent layers such that the stacking direction of the C phase determines the stacking direction of the IC phase. From this follows that the nucleation of the IC-CDW is inherently three dimensional (3D). We observe the activation of a coherent shear mode in the optically driven transitions to the transiently stabilized unreconstructed phase. The activation mechanism starts with a rapid lifting of the periodic lattice distortions (PLD) of the Ta sublattice which results in formation of local transient velocity disparities in the Se sublattice. The local differences in Se-phonon amplitudes result in noncompensated shear forces between the layers. This is an example of a multistep coherent launching mechanism. The energy of the optically excited electronic state dissipates energy into modes of the PLD through strong electron-phonon coupling. The rapid suppression of the PLD launches the third step, a coherent vibrational shear mode with low dissipation. The results highlight the importance in considering the 3D nature of the CDWs in the analysis of both structure and dynamics in transition-metal dichalcogenides.

DOI: 10.1103/PhysRevB.101.094303

I. INTRODUCTION

Two-dimensional (2D) materials are formed from extended covalently bonded crystalline sheets that may serve as building blocks for three-dimensional (3D) structures through stacking of the 2D sheets. The properties of the resulting 3D material are influenced by the weak interplane van der Waals bonds. A particularly exciting group of 2D materials are the transition–metal dichalcogenides (TMDs) that exhibit intriguing electronic and structural properties [1,2]. The formation of commensurate electronic charge-density waves (C-CDW) or incommensurate electronic charge-density waves (IC-CDW) and their relation with periodic lattice distortions (PLD) have been the subject of particular interest [3–6]. The strong electron-phonon coupling makes these systems especially well suited for studies of quasiparticle interactions [7] and photo-driven phase transitions [8]. Under the assumption of a weak interplane coupling in TMDs, most previous studies have restricted the analysis of the PLD to the two-dimensional superstructure within the layers. However, the ground states of several 2D CDW materials exhibit a complex three-dimensional structure with a preferential stacking order in the out of plane direction [9]. An increasing number of theoretical and experimental studies have demonstrated the importance in including the interplane van der Waals interactions in the description of the physical properties of layered materials [10–13]. In a time-resolved diffraction study by Erasmus *et al.* [14], it was shown that strong out of plane coupling facilitates CDW formation and that 3D properties should be considered in analysis of the formation of periodic lattice distortions in TMDs. Other studies have predicted how a change in stacking order may result in metal to semiconductor transition or interlayer exciton formation [10,11].

The combination of a CDW and long-range stacking order in 1*T*-$TaSe_2$ makes it a prime candidate for studying the coupling of the in-plane PLD with the interlayer van der Waals interaction [9,15]. The formation of a long-range stacking order indicates the significance of the interlayer interaction on the 3D properties of the material. The C-CDW phase of 1*T*-$TaSe_2$ hosts 13 in-plane Ta atoms displaced from their unreconstructed lattice positions to form a so-called Star of David cluster with a hexagonal $\sqrt{13}a_0 \times \sqrt{13}a_0$ superstructure, as shown in Fig. 1 [3,16]. The C in-plane superlattice exhibits a 13.9° rotation relative to the unreconstructed lattice. Results from diffraction and nuclear magnetic resonance have determined that the C-CDW of 1*T*-$TaSe_2$ exhibits a

*jonas@kth.se

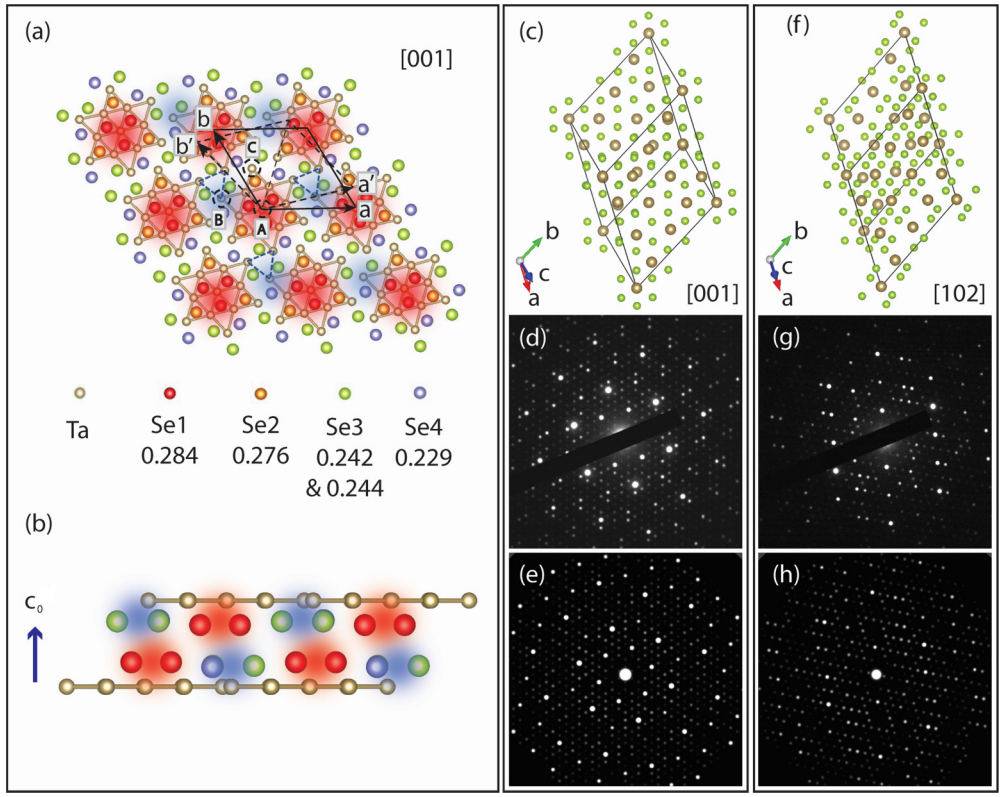

FIG. 1. (a) Illustration of superstructure and stacking arrangement in $1T$-$TaSe_2$. The periodic lattice displacements form a 13-Ta atom Star of David cluster (illustrated by solid bonds). The **a** and **b** vectors indicate the C-CDW unit cell and the **a′** and **b′** vectors the IC-CDW unit cell. Blue dashed triangles indicate the threefold symmetric stacking displacements. Se atoms are color coded according to their c-axis coordinate (in fractions of c) as listed in the lower part of (a). The Se atoms at the center of a Star of David cluster are at highest (most protruding, red-shaded areas) positions. The buckling of the Se layer results in a $2\mathbf{a_0}$ translation vector as the Star of David center on an adjacent layer will locate above positions where Se atoms are at the lowest positions (blue-shaded areas). (b) Stacking arrangement along the $\mathbf{c_0}$ direction for two adjacent layers of the C-CDW phase. Only Se atoms between the Ta layers are included. Projections of the commensurate phase at (c) [001] and (f) [102] zone axis (as indexed by the unreconstructed phase) and the corresponding experimental diffraction patterns in (d) and (g), respectively. The simulated diffraction patterns along [001] (e) and [102] (h) are in excellent agreement with the experimental result. At the [102] zone axis, one (out of three) stacking shift direction is placed in bright Bragg diffraction condition.

$T_i = 2\boldsymbol{a_0}$ translation vector between subsequent layers, with a threefold rotational symmetry [17–20]. The three symmetric translation directions are not randomly populated, instead $1T$-$TaSe_2$ exhibits a long-range stacking order indicating interactions extending even to next-nearest layers [15]. After a $\mathbf{c_0}$-axis period of 13 layers the in-plane atomic positions will reside in equivalent positions to the first layer of the stack.

$1T$-$TaSe_2$ exhibit a commensurate to incommensurate CDW phase transition at $T_c = 473$ K [16]. The superlattice of the IC-CDW phase rotates 13.9° relative to the C-CDW phase to align with the unit-cell vectors of the unreconstructed lattice and forms a fcc-like out of plane stacking [9]. The fcc-like stacking minimizes the electrostatic interaction between the in-plane triangular charge-density lattices [21,22]. A detailed structural description of the change in stacking at the C-IC phase transition may contribute to the understanding of the correlation between the intralayer structure and the interlayer van der Waals interaction in TMDs. An understanding of this correlation may shed light on the processes that underpin the many intriguing fundamental properties of this class of materials such as the long-lived metastable state in $1T$-$TaSe_2$ [23], hidden states in $1T$-TaS_2 [24], and the relation between CDW and superconductivity [25].

Ultrafast electron diffraction has successfully been employed in studies of photo-driven intraplane structural dynamics in TMDs [8,14,26–28]. Recently, Le Guyader *et al.* [29] extended the scope of analysis to include dynamics in stacking order of $1T$-TaS_2. The large Se $4p$-Ta $5d$ transfer interaction in $1T$-$TaSe_2$ results in a well-established 3D Fermi surface. From the 3D electronic structure follows a stronger interlayer interaction and higher degree of long-range order compared to $1T$-TaS_2 [30,31]. Furthermore, the phase diagram of $1T$-$TaSe_2$ has an additional advantage over $1T$-TaS_2, in that it does not include the rather complicated nearly commensurate phase. All taken together makes $1T$-$TaSe_2$ a well-suited model system for studies of the influence of interlayer interaction on transient structure dynamics. Here, we investigate the 3D structural dynamics in $1T$-$TaSe_2$ during a photo-driven CDW transition and subsequent recovery by means of ultrafast electron diffraction. Information of the stacking order is accessed by application of precise sample

tilt angles to selected zone axes. The dynamics of the C-IC CDW phase transition and the change in out of plane stacking order in conjunction with the phase transition is described. A coherent shear phonon is observed following a photo-driven suppression of the C-CDW. The excitation of the shear phonon is explained through a mechanism including residual interlayer forces originating from Se sites at different corrugation amplitude (out of plane displacement) in combination with the break of symmetry resulting from the alternating rotational directions in stacking order.

II. METHODS

A. Experiment

Single crystals of $1T$-$TaSe_2$ were grown from high-purity elements by a chemical vapor transport method using iodine as transport agent [32]. Transmission electron microscopy (TEM) samples were carefully microtomed at the preferential cleave plane using a diamond knife and were placed on a single-layer graphene TEM grid (Ted Pella). The sample thickness was measured, on the grid, to be 20 nm using a JPK NanoWizard 3 atomic force microscope (Supplemental Material, Fig. S1 [33]). Electron-energy-loss spectroscopy confirmed the thickness as 20 nm (Supplemental Material, Fig. S1 [33]). Variable-temperature electron diffraction experiment was performed using a Gatan double-tilt heating holder (model 652). Time-resolved diffraction experiments were performed in an ultafast electron microscope described in detail in Ref. [34]. Briefly, the instrument is a modified JEOL JEM 2100 TEM with a conventional thermionic electron gun operating at 200 keV. All the time-resolved experiments were performed at room temperature. The electron bunches were generated through photoemission by a UV (258 nm, Amplitude Systemes) laser pulse. The full width at half maximum (FWHM) of the electron bunches was approximately 1.2 ps as characterized by photo-induced near-field electron microscopy (Fig. S2 [33]) [35]. Each electron bunch contains approximately 1000 electrons. The sample was excited by a coupled 300-fs (Amplitude Systemes) 515-nm laser pulse ($hv = 2.4\,\mathrm{eV}$) focused to a spot on the sample with a FWHM of 120 μm. The sample was excited at a repetition rate of no more than 70 kHz to allow for complete relaxation between excitation pulses. No sample degradation or twin domain formation was observed in the analysis.

Diffraction patterns were simulated using CRYSTAL MAKER SINGLECRYSTAL 3 with intensities estimated from the structure factor under a kinematic assumption. The analysis used atomic structure information of the commensurate phase from Brouwer and Jellinek [19]. A 39-layer cell was constructed in order to consider the coexistence of threefold rotational-oriented domains in out of plane direction (Fig. S3). The atomic structure models were drawn by VESTA [36].

B. Simulations

1. Total energies and phonons

The total energy calculations used to assess the stacking order were performed with the VASP software and similar plane-wave and energy cutoffs as used for the phonon calculations. The Brillouin zone was sampled by a $\mathbf{\Gamma}$-centered $3 \times 3 \times 6$ mesh of k points. The supercell was set up in the C-CDW phase with a translation vector $\mathbf{2a_0}$, in accordance with Fig. 1(a).

2. Band structure and optical absorption

The band-structure calculations and the calculation of the joint density of states to assess the momentum-resolved optical absorption across the Brillouin zone were performed using the ELK code [37]. The cutoff for the plane-wave basis functions was determined by setting the maximum $|\vec{G} + \vec{k}| \cdot R_{MT}$ to 9, where R_{MT} is the average radius of the augmentation muffin tins, $\vec{G}$ is a reciprocal lattice vector, and $\vec{k}$ a crystal momentum within the first Brillouin zone. We used a $\mathbf{\Gamma}$-centered $3 \times 3 \times 3$ mesh of k points to sample the Brillouin zone for the self-consistent density, followed by a band-structure calculation along the high-symmetry lines as specified in Fig. S13.

3. Shear phonon

The first-principles calculation of the phonon modes used to identify the shear-mode excitation was performed using density-functional theory implemented using the projector-augmented waves method in the VASP code [38,39]. The exchange and correlation was treated with the density functional by Hamada, with explicit inclusion of van der Waals interactions [40]. A cutoff of 500 eV was used for the plane-wave basis, and an energy convergence criterion of 1×10^{-9} eV in order to capture the weak energy dispersion of the interlayer shear modes in a finite-displacement framework. The Brillouin zone of a 12-atom supercell consisting of 4 vertically stacked unit cells of $1T$-$TaSe_2$ in the unreconstructed phase was sampled by a $12 \times 12 \times 6$ mesh. The time-dependent density-functional theory (TD-DFT) coupled to Ehrenfest molecular-dynamics simulations was performed with the TDAP package implemented on top of the SIESTA software [41,42]. Norm-conserving pseudopotentials were used together with a double-zeta+polarization basis set for computational efficiency. The exchange-correlation potential was treated within the adiabatic approximation using the functional by Perdew, Burke, and Ernzerhof [43]. A supercell composed of two unit cells of $1T$-$TaSe_2$ in the C-CDW phase, consisting of 156 atoms, was used in order to allow for sufficient lattice dynamics. Additional details are provided in the Supplemental Material [33].

III. RESULTS AND DISCUSSION

This section begins with a description of the static structures of the commensurate and incommensurate CDW phases of $1T$-$TaSe_2$, with an emphasis on the structural properties central to establishing the out of plane stacking order. It is followed by results from a thermally driven phase transition demonstrating the strong influence of a change in PLD and stacking order on the experimental diffraction patterns. These results lay the framework for the interpretation of the processes included in the photo-driven transition, especially the fast change of stacking order and the excitation of a shear phonon.

A. Structural model

Figure 1(a) illustrates the in-plane atomic structure of the commensurate CDW phase of $1T$-$TaSe_2$ projected along the [001] direction with the Se atoms color coded according to their relative coordinate along the c axis of the C-CDW phase (in fractions of c) [19]. For clarity of presentation of the PLD-induced buckling of the Se atoms only the top-layer Se atoms are included in the figure. Red-shaded circular regions indicate the most protruding, convex, sites of the layer. Conversely, blue-shaded circular regions indicate concave sites. In the stacking of layers it is energetically favorable for convex protruding positions to reside above concave positions in adjacent layers as revealed in Fig. 1(b), resulting in a stacking translation vector of $T_i = 2\mathbf{a_0}$ [18]. The transition to the IC phase results in a rotation of the unit cell of the superstructure from (**a,b**) to a direction parallel to the fundamental lattice (a',b') [Fig. 1(a)]. In the IC phase the layer stacking order is fcc-like; thus the Star of David cluster will form an ABC stacking in the out of plane direction.

Figures 1(c) and 1(f) show projections of the commensurate phase superstructure at the [001] and [102] zone axes (as indexed by the unreconstructed phase). Figure 1 shows experimental diffraction patterns along the [001] [1(d)] and [102] [1(g)] zone axes. Combined experimental and structural consideration suggests that alignment of the sample to the [001] zone axis place the superstructure satellite spots out of bright Bragg diffraction conditions. The experimental intensity at satellite positions may be explained as result from formation of Bragg rods. However, the observed experimental intensity of the satellite spots is significantly stronger than what is expected from a stacking sequence extending throughout the entire 20-nm thickness of the sample. This implies that the sample must include rotational domains in the out of plane direction. Figures 1(e) and 1(h) show simulated diffraction patterns from a 39-layer-thick unit cell including 13 layers from each of the 3 symmetric stacking directions along the [001] and [102] directions. The complete unit cell is shown in Fig. S3. Tilting the sample to the [102] zone axis of the unreconstructed phase places specific planes of the superstructure in bright Bragg condition. This results in stronger diffraction of selected satellite spots, as shown in Fig. 1(g). The experimental and simulated diffraction patterns are in good agreement, indicating that the structure used for the simulation is reasonable. The [102] zone axis allows for tracking changes in the three-dimensional superstructure, including changes of stacking order at the C-IC phase transition. It is worth to point out that only one stacking shift direction is placed in bright Bragg diffraction condition at the [102] zone axis. The other two symmetric translation vectors are accessed at equivalent zone axes [012] and $[\bar{1}\bar{1}2]$. All three translation vectors exist in the sample. Diffraction patterns collected at two symmetric zone axes that place symmetric stacking shifts in conditions for bright Bragg diffraction are shown in Fig. S5.

B. Thermal-driven commensurate to incommensurate transition

Diffraction patterns of the C-CDW and the IC-CDW phases were collected along the [102] zone axis as a function of temperature. Figure 2(a) shows a diffraction pattern from the C-CDW phase acquired at 423 K and Fig. 2(b) the corresponding pattern from the IC-CDW phase collected at 503 K. From a comparison of the diffraction patterns it is evident that the main lattice Bragg spots remain in similar positions while the satellite spots that stem from the superstructure change dramatically. Figures 2(e) and 2(f) show magnified views of the areas enclosed by the red-dashed circles in Figs. 2(a) and 2(b). Figure 2(g) shows the subtracted diffraction intensity for the two phases. The rotation of spots is evident from the results, as is the elimination of some spots. At the C-CDW to IC-CDW transition temperature the q_C^1 satellite spots in Fig. 2(e) rotate 13.9° to the q_{IC}^1 positions in Fig. 2(f), while q_C^2 disappear without a corresponding spot appearing at the q_{IC}^2 position. This implies that q_{IC}^1 is placed in bright Bragg diffraction condition at the [102] zone axis while q_{IC}^2 is out of Bragg condition. This difference in diffraction condition for the q_{IC}^1 and q_{IC}^2 satellite spots can be traced from the three-dimensional superstructure of the IC-CDW phase. Figure 2(c) shows the intensity of the q_C^1 and q_{IC}^1 satellite

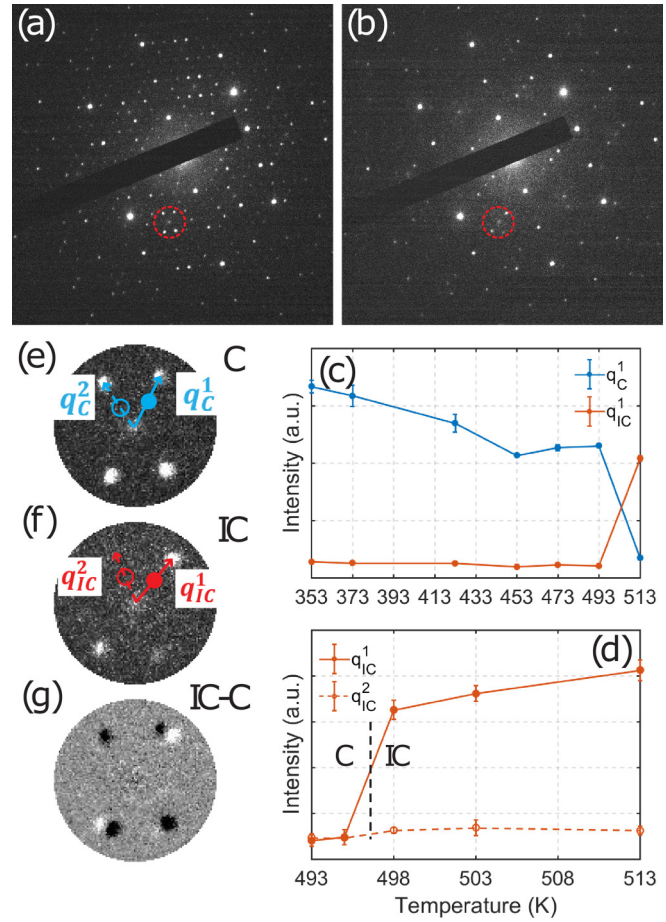

FIG. 2. Diffraction patterns collected along the [102] zone axis of the C-CDW phase at 423 K (a) and of the IC-CDW phase at 503 K (b). Enlarged diffraction patterns of the areas indicated by the red-dashed circles in (a) and (b) are shown in (e) and (f). (g) shows the subtracted (f)−(e) diffraction pattern. (c) The intensity of q_C^1 and q_{IC}^1 as a function of temperature, across the C-IC transition, and (d) the temperature-resolved intensities of q_{IC}^1 and q_{IC}^2 at temperatures close to the transition.

spots as a function of temperature, across the C-CDW to IC-CDW phase transition. The intensity of q_C^1 decreases steadily with temperature below the phase transition. In the same temperature range, there is no intensity at the q_{IC}^1 position. The q_C^1 spot disappears immediately above the transition temperature. Simultaneously we observe a dramatic increase in the intensity of q_{IC}^1, to levels similar to what was observed for q_C^1 at temperatures below the transition. Detailed traces of the intensity of q_{IC}^1 and q_{IC}^2 as a function of temperature are shown in Fig. 2(d). At the transition temperature of approximately 498 K the intensity of q_{IC}^1 increases dramatically compared to q_{IC}^2. This implies that both the in plane superstructure and the out of plane stacking order change simultaneously at the transition, suggesting that the three-dimensional character of the IC-CDW phase is immediately established above the transition. This will be further investigated in the time-resolved photoinduced phase transition studies below. Note that the temperature in Fig. 2 is measured at the sample holder position which may be slightly higher than the actual temperature of the sample. The continued increase in intensity of the q_{IC}^1 with temperature above the transition may be a result of a domain growth process. This interpretation is corroborated by a slight decrease in satellite spot width at increasing temperature.

C. Photo-driven commensurate to incommensurate transition

Next, we will discuss the photoinduced transient structural changes in $1T$-$TaSe_2$. In the C-CDW phase, electronic-structure calculations indicate that absorption occurs predominantly by transitions from p states on Se to d states on Ta [44]. The electronic bands in the C-CDW phase do not cross the Fermi level along any of the high-symmetry directions in the in plane of the layers. However, there are band crossings between **Γ**-***A*** and ***L***-***M*** that in the hexagonal Brillouin zone correspond to the out of plane direction. This is indicating that charge transport along the stacking direction is more favorable than in the planes (Supplemental Material, Fig. S13 [33]). This band structure is similar to TaS_2 that also shows no band crossings in the planes, but in the out of plane direction. [10] The suppression of the PLD starts already within the duration of the optical pump pulse; this fast initiation is warranted by the strong electron-phonon coupling between the photoexcited electrons, as can be deduced from the strong dependence of the band energies to the amplitude of the mode responsible for the PLD as seen in Fig. S13. During the melting process of the PLD, additional intraplanar electronic band crossings of the Fermi level appear, allowing for a more efficient recombination of electrons and holes. In order to estimate where in the Brillouin zone the optical pump will introduce the majority of electron-hole pairs, we calculate the absorption probability as a function of crystal momentum. To model the absorption, we calculate the joint density of states for a range of PLD amplitudes. For a photon energy of approximately 2.4 eV we deduce that the absorption in the C-CDW phase allows for absorption in a large part of the Brillouin zone for the pump photon energy under consideration. The increased band dispersion resulting from the melting of the PLD leads to absorption in a wider energy range. The initial stages of the melting of the PLD are likely different for optical and thermal melting. This can be inferred from the

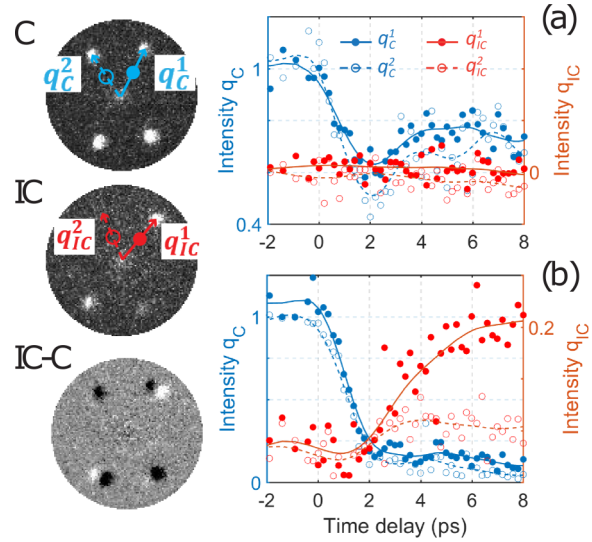

FIG. 3. (a), (b) Time dependence of the diffraction intensity of the satellite clusters of the commensurate and incommensurate phases. The legends of the traces (q_C^1, q_C^2, q_{IC}^1, and q_{IC}^2) are indicated in the diffraction patterns to the left, where the top panel shows the C-CDW before time zero, the middle panel the IC-CDW phase after time zero, and the lower panel the difference pattern for the two phases. The laser pump fluences in (a) and (b) were 1.4 and 2.5 mJ/cm^2, respectively.

computed momentum-resolved optical absorption probability, as seen in Fig. S13. For an energy range of about 2.4 eV we can see that, in the initial phase, we have optical absorption throughout the Brillouin zone. As the PLD is suppressed and the unreconstructed structure is restored to the lattice, the electronic bandwidth increases. An increased degeneracy in specific parts of the Brillouin zone also indicates the increase in symmetry. Similarly, we can, by looking at the evolution of the band structure, see that upon thermal melting we will have the initial thermal excitations of primarily intraband character in a very limited portion of the Brillouin zone, between **Γ** and ***A*** Please note that it is the first Brillouin zone of the $1T$ structure in the C-CDW phase that is depicted; for clarity the same representation is also used in the unreconstructed phase. We expect that the differences along the course of the melting have an impact on transient properties whereas the final stage is similar.

Figures 3(a) and 3(b) show the transient intensity of the superstructure satellite spots along the [102] zone axis for the C and IC phases following excitation by a 515-nm laser pulse. The corresponding results for the [001] zone axis are shown in Figs. S7 and S8 [33]. In Fig. 3(b) the pump fluence (2.5 mJ/cm^2) was sufficient to drive the sample across the C-IC CDW phase transition as observed from the increase in intensity of the satellite spots associated with the IC phase, while in Fig. 3(a) the fluence (1.4 mJ/cm^2) was kept below the onset for IC formation. In both cases the satellite spots of the C-CDW phase show a constant diffraction intensity before time zero. At time zero, at the time of excitation of the sample, the intensity of the commensurate satellite spots decreases instantaneously (convoluted by the instrumental time resolution). The PLD is suppressed already during

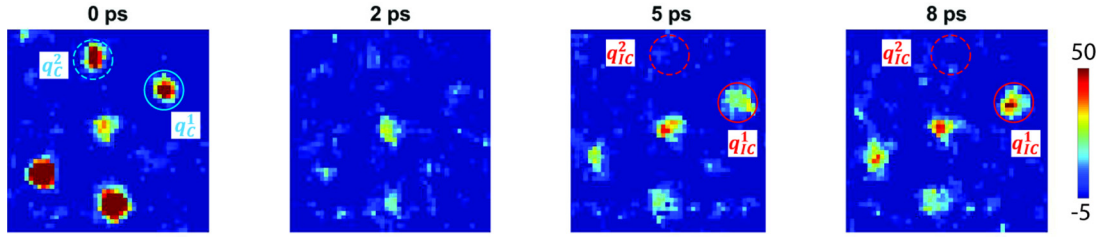

FIG. 4. Time-resolved diffraction patterns illustrating the change in superstructure satellite spot intensity and position following 515-nm excitation at 2.5-mJ/cm^2 fluence. Collected at the [102] zone axis.

the electronic relaxation process due to the strong electron-phonon coupling between the photoexcited states and the PLD mode. This process tentatively happens within a single oscillation period of the PLD amplitude mode, or less than 300 fs [8,26]. No apparent change in intensity is observed at positions corresponding to q_{IC}^1 and q_{IC}^2 for a laser excitation fluence of 1.4 mJ/cm^2 [Fig. 3(a)]. Instead a partial recovery from the transient unreconstructed phase can be observed at the q_C^1 and q_C^2 positions. The transient results allow for extraction of a 0.7-ps recovery time constant for the C-CDW and the starting point for the recovery is estimated to ∼1.3 ps (Supplemental Material, section 2.1 [33]). The recovery time constant is marginally shorter than that observed in $1T$-TaS_2 (∼4 ps) [8] but significantly shorter than in the weakly interlayer interacting $4Hb$-$TaSe_2$ (∼150 ps) [14]. These results indicate that stronger interlayer interaction results in shorter recovery times of the C-CDW. At 2.5-mJ/cm^2 pump fluence, the onset for formation of the diffraction spots associated with the nucleation of the IC phase is observed approximately ∼1 ps after time zero [Fig. 3(b)]. The 1-ps delay between the extinction of the C phase and the emergence of the IC phase directly implies that the transition involves a transient phase with a completely suppressed PLD, with a structure similar to an unreconstructed $1T$ phase. Figure 3 traces the change in q_{IC}^1 and q_{IC}^2 intensities individually as filled and empty circles. The observed onset time is similar for both satellite spots and the same timescale is observed for establishing the IC-CDW phase along the [001] zone axis (Supplemental Material, Figs. S7 and S8). A 1-ps delay time before nucleation of the IC-phase is approximately twice the period of the CDW amplitude mode reported at 2.4 THz for $1T$-TaS_2 [45,46], and implies that a phononic thermalization is involved in the decay of this highly perturbed photoinduced state before the onset of incommensurate phase formation. A tentative thermalization pathway may involve the longitudinal acoustic mode that in $NbSe_2$ and TaS_2 has been associated with the thermally driven CDW transition [47–49]. A softening of this mode to ∼1 THz has been reported close to the CDW transition in TaS_2 [49], a period similar to the ∼1-ps delay observed for the onset of IC-CDW formation in the photo-driven experiments here.

At times immediately following the delayed onset of the IC phase we note that the change in intensity of the q_{IC}^1 and q_{IC}^2 satellite spots do not exhibit the same transient behavior. q_{IC}^2 show a minor increase in intensity up until 4 ps while the temporal trace of q_{IC}^1 shows a continued increase in intensity also after this point in time. After 4 ps the temporal traces for q_{IC}^1 and q_{IC}^2 qualitatively resemble the temperature traces from Fig. 2(d) except that the intensity of the q_{IC}^1 at 8 ps is only 20% of the intensity of q_C^1 before time zero. The relative diffraction intensities deviate from the thermal-driven phase transition where the intensity of q_{IC}^1 above and q_C^1 below the transition temperature are similar, as shown in Fig. 2(c). The deviation of the transient diffraction intensity from the steady state implies that the atomic structure has yet to reach its equilibrium positions and may be explained by a process of domain growth that is expected to persist on the nanosecond timescale [50]. The development of individual CDW satellite diffraction spots at selected time delays are shown in Fig. 4. Already at 5 ps we observe significantly higher diffraction intensity at the position of q_{IC}^1 compared to the position of q_{IC}^2 and at 8 ps the diffraction pattern is qualitatively rather similar to the steady-state pattern shown in Fig. 2(f). A weak spot at the center-inverted position to q_{IC}^2 is observed in both Fig. 2(f) and Fig. 4 that probably stems from a slight misalignment of the sample from the [102] zone axis. The divergence of the q_{IC}^1 and q_{IC}^2 intensities at around 4 ps allows us to reach the conclusion that the stacking order of the IC phase has been initiated already at this point, a manifestation of the strong coupling between the layers of $1T$-$TaSe_2$. The rapid formation of IC-phase stacking order indicates that local nucleation of IC-phase PLD within the $TaSe_2$ $TaSe_2$ layers is influenced by the positions of the Star of David clusters in adjacent layers such that the stacking direction of the IC-CDW phase is decided by the previous C-CDW phase stacking direction of the domain. From this follows that the nucleation of the IC-CDW is three dimensional. Our DFT modeling did not find an energy difference of the three symmetric stacking directions in the commensurate phase that may explain a preferred stacking direction (Supplemental Material, sec. 3.1). Therefore, an explanation for preservation of stacking direction throughout the complete C-IC-C excitation and relaxation cycle is interpreted to stem from kinetical restrictions. Under our experimental conditions we did not observe any change in C-CDW phase rotation chirality (clockwise or anticlockwise rotation of the in-plane angle of the C-PLD relative to the unreconstructed phase) or laser-induced formation of mirror domain walls as has been reported for high pump fluence in the nearly commensurate phase of $1T$-TaS_2 [51]. Wiegers *et al.* [18] have previously reported a correlation between the rotation chirality and stacking translation direction in the C phase of $1T$-$TaSe_2$. This was explained by the strong interlayer interaction in $1T$-$TaSe_2$ in combination with small distortions in the Star of David cluster that minimize the interlayer strain for a single stacking direction within a domain.

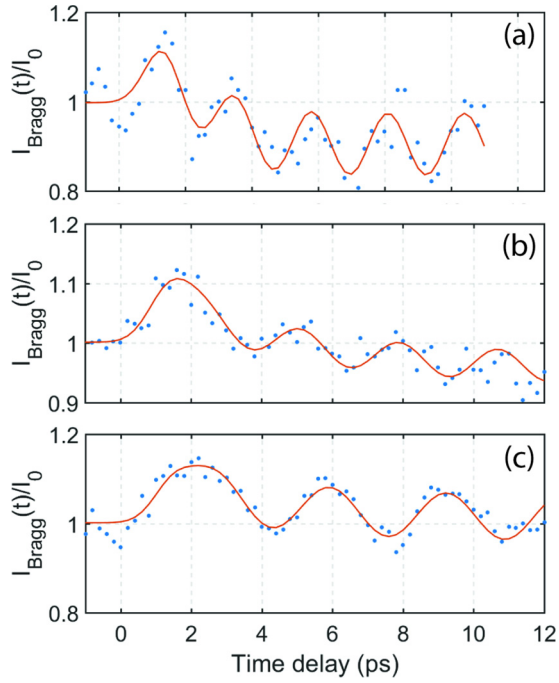

FIG. 5. Temporal traces of average Bragg diffraction spots intensity in $1T$-$TaSe_2$ at increasing laser pulse fluence: (a) 1.3 mJ/cm^2, (b) 2.0 mJ/cm^2, and (c) 2.4 mJ/cm^2. A softening of the shear phonon is observed with extracted frequencies at 0.43, 0.36, and 0.30 THz, respectively. A phase transition to IC-CDW is observed for the fluencies in (b) and (c), while the fluence in (a) results in a relaxation to the C-CDW from the transiently unreconstructed state.

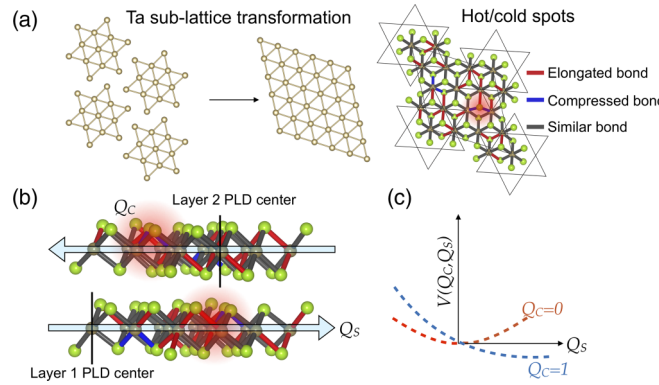

FIG. 6. Time decomposition of the events leading to the launching of the shear mode. The optical pump immediately initiates a suppression of the PLD in the Ta sublattice, as shown in (a). After melting, there are remnant effects of the Se-layer bond oscillations in terms of a difference in velocity for Se atoms situated at different locations within the C-CDW unit cell. On the right-hand side of panel (a), the Ta–Se bonds are color coded according to bond-compression/elongation with respect to the $1T$-unreconstructed state Ta–Se bond, a compression of 5% or more is colored blue, and an elongation of similar magnitude is colored red. At the edge of the Star of David cluster the bond-length disparity between Ta and Se atoms is large, as indicated by the red-shaded region on the right-hand side of panel (a), where a strong bond compression and bond elongation to the same Se atom is seen. Panel (b) shows how locations with high Se velocities are related for the stacking sequence of the calculation. Similar to panel (a), the bonds are colored with respect to the deviation to the unreconstructed-state bond length. The arrows indicate the direction of the forces. Panel (c) shows a schematic view of the potential-energy surface and the dependence on the coordinates Q_s and Q_c. When $Q_c = 1$, the energy is decreased by launching the shear mode. The PLD that is present in the C-CDW phase pins the starting position to be roughly $Q_c = 1$ (depending on the phase of the lattice vibrations in the system).

D. Excitation of shear phonon

Immediately following excitation, the Bragg spots of the main lattice increase in intensity simultaneously with the suppression of the C-CDW. This is in agreement with what has been reported for similar CDW materials [8]. After 1–2 ps the main lattice Bragg peaks will again decrease in intensity due to reestablishment of the PLD (either C or IC) combined with heating of lattice (the Debye-Waller effect). More interestingly, in $1T$-$TaSe_2$, we also observed a slow intensity oscillation of the main Bragg peaks following photoexcitation. The individual diffraction spots show an in-phase change as demonstrated in Fig. S6. The average intensity oscillation at different pump power is shown in Fig. 5. The procedure for fitting of the experimental data is described in the Supplemental Material, sec. 2.2. From the fitting procedure, which includes the temporal resolution, we may extract the oscillation frequencies as 0.43, 0.36, and 0.30 THz for 1.3, 2.0, and 2.4 mJ/cm^2, respectively (Fig. 5). The oscillation is interpreted as excitation of a phonon and the softening observed at increased fluence is consistent with an anharmonic response at large excitation amplitudes [52]. A redshift can also be expected with increasing sample temperature. For a 1.3-mJ/cm^2 pump fluence [Fig. 5(a)] no C-IC phase transition was observed, while excitation using pump fluencies of 2.0 and 2.4 mJ/cm^2 results in observation of IC phase formation [Figs. 5(b) and 5(c)]. The persistence of the intensity oscillation in the IC phase indicates that a similar phonon exists in both phases. A careful analysis of the Bragg intensities at high pump fluence reveal a temporal broadening of the first peak after time zero. The broadening is however not symmetric, instead the peak is observed to extend to longer temporal delays. The broadening may stem from slower relaxation processes of photoexcited electronic states at high pump power [53] or stabilization of the transient unreconstructed state as discussed in connection with Fig. 3(b). The starting point of the oscillation is also delayed at high fluence according to the parameters extracted from the fitting process (see Supplemental Material, sec. S2 for more details [33]). In order to assess the intensity oscillations of the Bragg spots, we performed first-principles calculations of phonon frequencies in the C-CDW phase. The outcome shows that in principle only shear modes appear in the corresponding frequency range, 0.46 THz according to calculations. The frequency is very close to the observed value at low pump power as shown in Fig. 6(a). An assessment using a sound velocity of ∼2000 m/s [54] and the sample-thickness (∼20 nm, Supplemental Material, Fig. S1) rules out breathing modes (with resulting periods of $T = 20$ ps). Through modulation of the lattice with the shear mode in the stacking direction we may calculate the corresponding structure factor change as a function of shear displacement. The simulated diffraction intensities reproduce the experimental intensity

oscillations (Fig. S10). As indicated by the analysis, this mode is almost undamped during the timescales probed here. This indicates a coherent motion, albeit with a delayed onset from the pump pulse. In the following, we analyze the underlying mechanism for the coherence and onset.

Upon melting of the PLD, the Ta sublattice is believed to quickly attain unreconstructed phase positions. However, as indicated by our TD-DFT simulations, the dynamics carry remnant features of the PLD, namely the amplitude of the vibrational modes, as visualized in Fig. 6. We investigate the effect of these remnant features using first-principles calculations for a two-layer model of the material.

We perform a simulation of $1T$-$TaSe_2$ (see Supplemental Material for details) using time-dependent density functional theory coupled to molecular dynamics, as implemented in the TDAP code [41]. The simulation is started from a completely relaxed structure in the C-CDW phase. The external field is introduced as a vector potential in the Hamiltonian, exciting the electrons primarily from Se-p to Ta-d states (see Fig. S14 for details). The first 130 fs of the trajectory indicates a large velocity disparity between Se atoms (and Ta atoms), indicating that the Se atom with the largest deviation from the ideal bond lengths have a higher velocity. Note that only one layer of material is simulated using the TD-DFT framework due to the computational complexity, hence the stacking vector is $T_\mathrm{i} = 0$. The use of a single layer introduces additional symmetries that are in the real material broken by the stacking order. The result of the TD-DFT simulation ties the bond-length disparity of Se atoms to the velocity as a function of time.

We then proceed with static modeling of a two-layer shear displacement in a hexagonal stacking mimicking the stacking vector $T_\mathrm{i} = 2\mathbf{a_0}$ of the trigonal phase. The stacking order is such that the center of the Star of David cluster in the adjacent layers will be situated directly on top of a local region with high Se velocities (Fig. 6). The center Ta atom itself has in fact a Ta–Se bond length similar to those in the unreconstructed $1T$ phase. The shear-mode displacement vector is represented by Q_S The bond-length disparity of Se atoms that leads to different velocities for different Se atoms is represented as a collective mode with displacement vector Q_C indicating the bond distortions inherent to the C-CDW phase. Q_C corresponds to a different local kinetic energy related to the Se-atoms' position in relation to the stacking order and the intralayer PLD.

Assume a potential-energy surface V of the form

$$V(\boldsymbol{Q_C}, Q_S) = \tfrac{1}{2}\boldsymbol{\omega_C^2 Q_C^2} + \tfrac{1}{2}\omega_S^2 Q_S^2 + \tfrac{1}{2}\boldsymbol{\gamma Q_C} Q_S + \mathrm{H.c.}, \qquad (1)$$

where ω_i represents frequencies and γ represents the linear coupling between the modes; H.c. represents higher-order corrections. The collective Se amplitude mode Q_C is not an eigenmode of the system, hence the vectorial form of the frequency. By modulating the amplitude of the Se atoms, we uncover a coupling to the shear mode indicating that $|\frac{dV}{dQ_s}| > 0$ when $|Q_C| > 0$, with the resulting force in the direction of the stacking order [Fig. 6(b)]. Note that for a perfect trigonal stacking the force will be compensated. However, our diffraction experiments indicate that the three equivalent stacking vectors are all present; hence, there will always remain uncompensated restoring forces from end points and layers in the vicinity of a transition in stacking-order direction. This will launch a coherent shear motion, that due to the weak coupling between the layers remains a coherent oscillation throughout the recovery of the CDW and PLD. Bear in mind that the coherent activation of the shear mode must occur within a half period, roughly 1 ps of time. Hence, the initial large velocity differences between different Se sites will launch the shear mode. The subsequent thermalization of the Se layer to a homogeneous temperature distribution will result in formation of a transient unreconstructed phase with reduced interlayer interaction that may contribute to a reduced decoherence rate of the shear excitation. This explains the initiation of the shear modes uncovered by the Bragg spot oscillations discussed in the previous section.

A thermally driven transition excites all phononic and low-lying electronic degrees of freedom in an incoherent manner. We do not see any signature of a homogeneous transition to the unreconstructed phase in our thermal excitation data, although it is not experimentally feasible to study the thermally driven transition on the picosecond timescale. An incoherent transition directly from commensurate to incommensurate phase will not result in a net force between the layers since local atomic displacements will be incommensurate, averaging out any resulting interlayer forces. This shows an important difference with respect to the optically induced transition, where the ultrafast coherently driven transition passes through the transient unreconstructed structure, resulting in an uncompensated net force between layers. However, the two processes reach similar end points on very long timescales.

IV. CONCLUSIONS

In summary, we report a detailed study of the transition between the C-CDW and IC-CDW phases of $1T$-$TaSe_2$ using both thermal and optical activation. Our results indicate that the C-CDW in $1T$-$TaSe_2$ is a highly three-dimensional entity due to strong interlayer interactions that establish long-range out of plane stacking order. Optical excitation results in suppression of the C-CDW on a subpicosecond timescale. A recovery time-constant of ∼0.7 ps is observed for the commensurate PLD at an optical pump power insufficient to drive a transition into the IC phase. The recovery time constant is shorter than what has been reported for the related compounds $1T$-TaS_2 and $4Hb$-$TaSe_2$. This may be rationalized as a result of the stronger interlayer coupling in $1T$-$TaSe_2$. At a laser pump fluence sufficient to optically drive nucleation of the IC phase is an ∼1-ps delay observed between the extinction of the C-CDW phase and the onset for formation of the IC-CDW phase, a manifestation of that the optically driven phase transition involves a transient unreconstructed state. The ∼1-ps delay time for the nucleation of the IC-CDW phase implies that a phononic thermalization is involved in the decay of this highly perturbed photoinduced transient state. Nucleation of an fcc-like stacking of the IC phase is observed already ∼4 ps after photoexcitation. Such rapid stacking order formation implies that the nucleation of the IC phase within the layers is influenced by the local geometry of the adjacent layers such that the stacking direction of the C phase determines the

direction of stacking in the IC phase. From this follows that the nucleation of the IC-CDW is inherently 3D. In the optically driven transitions to the transiently stabilized unreconstructed phase, we observe the activation of a coherent shear mode along the stacking direction. We analyze the launching mechanism in terms of locations with high and low velocities on the Se sublattice that result from the rapid melting of the PLD. The bond lengths of Se–Ta bonds in the C-CDW phase are related to the Se-atoms' position in the reconstructed lattice. During the melting, this results in differences in Se-phonon amplitudes, which results in noncompensated shear forces between the layers. This is an example of a multistep coherent launching mechanism. The energy of the optically excited electronic state dissipates energy into the PLD through the strong electron-phonon coupling. This rapid suppression of the PLD launches the third step, a coherent vibrational shear mode with low dissipation. Our results highlight the importance in considering the three-dimensional nature of the CDW in both structure and dynamics in $1T$-$TaSe_2$.

ACKNOWLEDGMENTS

This work was funded by the Knut and Alice Wallenberg Foundation and the Swedish Research Council (VR). S.J. gratefully acknowledges a stipend from the Chinese Scholarship Council. Dr. Miao Zhang is gratefully acknowledged for the sample thickness measurement by atomic force microscopy. Dr. Cheuk-Wai Tai is acknowledged for lending the *in situ* heating holder. O.G. acknowledges the Strategic Research Foundation (SSF) for funding through Grant No. ICA16-0037. Computational resources were provided by the National Supercomputing Center (NSC) through SNIC under Project No. 2018-3-221. O.G. would like to acknowledge Torbjörn Björkman and Jan Rusz for constructive discussions.

[1] S. Manzeli, D. Ovchinnikov, D. Pasquier, O. V. Yazyev, and A. Kis, Nat. Rev. Mater. **2**, 147 (2017).
[2] Q. H. Wang, K. Kalantar-Zadeh, A. Kis, J. N. Coleman, and M. S. Strano, Nat. Nanotechnol. **7**, 699 (2012).
[3] J. A. Wilson, F. J. Di Salvo, and S. Mahajan, Adv. Phys. **24**, 117 (1975).
[4] P. Bak, Rep. Prog. Phys. **45**, 587 (1982).
[5] P. Chen, W. W. Pai, Y.-H. Chan, A. Takayama, C.-Z. Xu, A. Karn, S. Hasegawa, M. Y. Chou, S.-K. Mo, A.-V. Fedorov, and T.-C. Chiang, Nat. Commun. **8**, 516 (2017).
[6] M. Porer, U. Leierseder, J.-M. Ménard, H. Dachraoui, L. Mouchliadis, I. E. Perakis, U. Heinzmann, J. Demsar, K. Rossnagel, and R. Huber, Nat. Mater. **13**, 857 (2014).
[7] T. Valla, A. V. Fedorov, P. D. Johnson, P.-A. Glans, C. McGuinness, K. E. Smith, E. Y. Andrei, and H. Berger, Phys. Rev. Lett. **92**, 086401 (2004).
[8] M. Eichberger, H. Schäfer, M. Krumova, M. Beyer, J. Demsar, H. Berger, G. Moriena, G. Sciaini, and R. J. D. Miller, Nature (London) **468**, 799 (2010).
[9] M. B. Walker and R. L. Withers, Phys. Rev. B **28**, 2766 (1983).
[10] T. Ritschel, J. Trinckauf, K. Koepernik, B. Büchner, M. v. Zimmermann, H. Berger, Y. I. Joe, P. Abbamonte, and J. Geck, Nat. Phys. **11**, 328 (2015).
[11] J. Kunstmann, F. Mooshammer, P. Nagler, A. Chaves, F. Stein, N. Paradiso, G. Plechinger, C. Strunk, C. Schüller, G. Seifert, D. R. Reichman, and T. Korn, Nat. Phys. **14**, 801 (2018).
[12] P. Ci, Y. Chen, J. Kang, R. Suzuki, H. S. Choe, J. Suh, C. Ko, T. Park, K. Shen, Y. Iwasa, S. Tongay, J. W. Ager, III, L.-W. Wang, and J. Wu, Nano Lett. **17**, 4982 (2017).
[13] K. F. Mak, J. Shan, and T. F. Heinz, Phys. Rev. Lett. **104**, 176404 (2010).
[14] N. Erasmus, M. Eichberger, K. Haupt, I. Boshoff, G. Kassier, R. Birmurske, H. Berger, J. Demsar, and H. Schwoerer, Phys. Rev. Lett. **109**, 167402 (2012).
[15] D. E. Moncton, F. J. DiSalvo, J. D. Axe, L. J. Sham, and B. R. Patton, Phys. Rev. B **14**, 3432 (1976).
[16] J. A. Wilson, F. J. Di Salvo, and S. Mahajan, Phys. Rev. Lett. **32**, 882 (1974).
[17] C. B. Scruby, P. M. Williams, and G. S. Parry, Philos. Mag. **31**, 255 (1975).
[18] G. A. Wiegers, J. L. de Boer, A. Meetsma, and S. van Smaalen, Z. Kristallogr. Cryst. Mater. **216**, 285 (2001).
[19] R. Brouwer and F. Jellinek, Physica B+C **99**, 51 (1980).
[20] M. Naito, H. Nishihara, and S. Tanaka, J. Phys. Soc. Jpn. **54**, 3946 (1985).
[21] K. K. Fung, J. W. Steeds, and J. A. Eades, Physica B+C **99**, 47 (1980).
[22] S. Tanda and T. Sambongi, Synth. Met. **11**, 85 (1985).
[23] X. Shi, W. You, Y. Zhang, Z. Tao, P. M. Oppeneer, X. Wu, R. Thomale, K. Rossnagel, M. Bauer, H. Kapteyn, and M. Murnane, Sci. Adv. **5**, eaav4449 (2019).
[24] L. Stojchevska, I. Vaskivskyi, T. Mertelj, P. Kusar, D. Svetin, S. Brazovskii, and D. Mihailovic, Science **344**, 177 (2014).
[25] B. Sipos, A. F. Kusmartseva, A. Akrap, H. Berger, L. Forró, and E. Tutis, Nat. Mater. **7**, 960 (2008).
[26] K. Haupt, M. Eichberger, N. Erasmus, A. Rohwer, J. Demsar, K. Rossnagel, and H. Schwoerer, Phys. Rev. Lett. **116**, 016402 (2016).
[27] S. Sun, L. Wei, Z. Li, G. Cao, Y. Liu, W. J. Lu, Y. P. Sun, H. Tian, H. Yang, and J. Li, Phys. Rev. B **92**, 224303 (2015).
[28] T.-R. T. Han, F. Zhou, C. D. Malliakas, P. M. Duxbury, S. D. Mahanti, M. G. Kanatzidis, and C.-Y. Ruan, Sci. Adv. **1**, e1400173 (2015).
[29] L. Le Guyader, T. Chase, A. H. Reid, R. K. Li, D. Svetin, X. Shen, T. Vecchione, X. J. Wang, D. Mihailovic, and H. A. Dürr, Struct. Dyn. **4**, 044020 (2017).
[30] K. Horiba, K. Ono, J. H. Oh, T. Kihara, S. Nakazono, M. Oshima, O. Shiino, H. W. Yeom, A. Kakizaki, and Y. Aiura, Phys. Rev. B **66**, 073106 (2002).
[31] M. Naito, H. Nishihara, and S. Tanaka, J. Phys. Soc. Jpn. **55**, 2410 (1986).
[32] F. J. Di Salvo, R. G. Maines, J. V. Waszczak, and R. E. Schwall, Solid State Commun. **14**, 497 (1974).
[33] See Supplemental Material at http://link.aps.org/supplemental/10.1103/PhysRevB.101.094303 for additional experimental results, methods for the analysis of time-resolved results, and computational details.

[34] S. Ji, L. Piazza, G. Cao, S. T. Park, B. W. Reed, D. J. Masiel, and J. Weissenrieder, Struct. Dyn. **4**, 054303 (2017).
[35] B. Barwick, D. J. Flannigan, and A. H. Zewail, Nature **462**, 902 (2009).
[36] K. Momma and F. Izumi, J. Appl. Crystallogr. **44**, 1272 (2011).
[37] K. Dewhurst, S. Sharma, L. Nordström, F. Cricchio, F. Bultmark, O. Granas, and H. Gross, elk FP-LAPW code, http://elk.sourceforge.net/ (2018).
[38] G. Kresse and J. Furthmüller, Comput. Mater. Sci. **6**, 15 (1996).
[39] G. Kresse and D. Joubert, Phys. Rev. B **59**, 1758 (1999).
[40] I. Hamada, Phys. Rev. B **89**, 121103(R) (2014).
[41] G. Kolesov, O. Grånäs, R. Hoyt, D. Vinichenko, and E. Kaxiras, J. Chem. Theory Comput. **12**, 466 (2016).
[42] J. M. Soler, E. Artacho, J. D. Gale, A. García, J. Junquera, P. Ordejón, and D. Sánchez-Portal, J. Phys.: Condens. Matter **14**, 2745 (2002).
[43] J. P. Perdew, K. Burke, and M. Ernzerhof, Phys. Rev. Lett. **77**, 3865 (1996).
[44] M.-T. Suzuki and H. Harima, J. Magn. Magn. Mater. **272-276**, E653 (2004).
[45] A. Mann, E. Baldini, A. Odeh, A. Magrez, H. Berger, and F. Carbone, Phys. Rev. B **94**, 115122 (2016).
[46] L. Perfetti, P. A. Loukakos, M. Lisowski, U. Bovensiepen, M. Wolf, H. Berger, S. Biermann, and A. Georges, New J. Phys. **10**, 053019 (2008).
[47] K. Schmalzl, D. Strauch, A. Hiess, and H. Berger, J. Phys.: Condens. Matter **20**, 104240 (2008).
[48] D. E. Moncton, J. D. Axe, and F. J. DiSalvo, Phys. Rev. B **16**, 801 (1977).
[49] Y. Machida, T. Hanashima, K. Ohkubo, K. Yamawaki, M. Tanaka, and S. Sasaki, J. Phys. Soc. Jpn. **73**, 3064 (2004).
[50] S. Vogelgesang, G. Storeck, J. G. Horstmann, T. Diekmann, M. Sivis, S. Schramm, K. Rossnagel, S. Schäfer, and C. Ropers, Nat. Phys. **14**, 184 (2018).
[51] A. Zong, X. Shen, A. Kogar, L. Ye, C. Marks, D. Chowdhury, T. Rohwer, B. Freelon, S. Weathersby, R. Li, J. Yang, J. Checkelsky, X. Wang, and N. Gedik, Sci. Adv. **4**, eaau5501 (2018).
[52] E. J. Sie, C. M. Nyby, C. D. Pemmaraju, S. J. Park, X. Shen, J. Yang, M. C. Hoffmann, B. K. Ofori-Okai, R. Li, A. H. Reid, S. Weathersby, E. Mannebach, N. Finney, D. Rhodes, D. Chenet, A. Antony, L. Balicas, J. Hone, T. P. Devereaux, T. F. Heinz, X. Wang, and A. M. Lindenberg, Nature (London) **565**, 61 (2019).
[53] L. Perfetti, P. A. Loukakos, M. Lisowski, U. Bovensiepen, H. Berger, S. Biermann, P. S. Cornaglia, A. Georges, and M. Wolf, Phys. Rev. Lett. **97**, 067402 (2006).
[54] M. S. Skolnick, S. Roth, and H. Alms, J. Phys. C: Solid State Phys. **10**, 2523 (1977).